Tribomechanical properties of hard Cr-doped DLC coatings deposited by low-frequency HiPIMS

J.A. Santiago, I. Fernández-Martínez, J.C. Sánchez-López, T.C. Rojas, A. Wennberg, V. Bellido-González, J.M. Molina-Aldareguia, M.A. Monclús, R. González-Arrabal

PII: S0257-8972(19)30871-0

DOI: https://doi.org/10.1016/j.surfcoat.2019.124899

Reference: SCT 124899

To appear in: *Surface & Coatings Technology*

Received date: 15 May 2019

Revised date: 7 August 2019

Accepted date: 9 August 2019

Please cite this article as: J.A. Santiago, I. Fernández-Martínez, J.C. Sánchez-López, et al., Tribomechanical properties of hard Cr-doped DLC coatings deposited by low-frequency HiPIMS, *Surface & Coatings Technology* (2019), https://doi.org/10.1016/j.surfcoat.2019.124899

Tribomechanical properties of hard Cr-doped DLC coatings deposited by low-frequency HiPIMS

J.A. Santiago[a,e,f], I. Fernández-Martínez[b], J.C. Sánchez-López[c], T.C. Rojas[c], A. Wennberg[b], V. Bellido-González[d], J.M. Molina-Aldareguia[a], M.A. Monclús[a], R. González-Arrabal[e,f]

a) IMDEA Materials Institute, c/Eric Kandel 2, 28906 Getafe, Madrid, Spain

b) Nano4Energy SL, José Gutiérrez Abascal 2, 28006 Madrid, Spain

c) Instituto de Ciencia de Materiales de Sevilla (CSIC-Universidad de Sevilla), Avda. Américo Vespucio 49, Isla de la Cartuja, 41092 Sevilla, Spain

d) Gencoa Ltd, 4 De Havilland Drive, Liverpol, L24 8RN, UK

e) Instituto de Fusión Nuclear "Guillermo Velarde" (Universidad Politécnica de Madrid), José Gutiérrez Abascal 2, 28006 Madrid, Spain

f) Departamento de Ingeniería Energética (ETSII/UPM), José Gutiérrez Abascal 2, 28006 Madrid, Spain

Keywords: HiPIMS, Diamond-like Carbon (DLC), hard coatings, nanostructures, metal-doped DLC, high-temperature tribology

Abstract

Cr-doped diamond-like carbon (Cr-DLC) films with Cr contents ranging from 3 up to to 20 at. % were synthesised in a codeposition process with HiPIMS (Cr deposition) and DC-pulsed technology (C deposition). The application of HiPIMS at low frequencies was observed to significantly enhance the energy density during the Cr plasma discharge due to the interaction of Cr-C species. The higher energy bombardment at low HiPIMS frequencies allowed doping with Cr the DLC structure avoiding the graphitization of the carbon structure. EELS spectroscopy was used to evaluate sp^3 content and Raman was used for sp^2 structural characterization of the films. Enhanced mechanical properties (hardness up to 30 GPa) were observed with nanoindentation for Cr-doped DLC at low frequencies. High temperature nanoindentation tests were also performed from room temperature to 425ºC in order to evaluate the evolution of hardness and Young Modulus with temperature. The results showed that the mechanical properties at high temperature mainly depend on the initial sp^3-sp^2 structure. Tribological tests were carried out in air from room temperature to 250ºC. Cr-doped DLC coatings deposited by low-frequency HiPIMS showed lower friction and wear compared to undoped DLC.

1. Introduction

Diamond like carbon (DLC) coatings have been recognized as one of the most valuable engineering materials for various industrial applications including manufacturing, transportation, biomedical and microelectronics. Among its many desirable properties, DLC stands out for its tribological properties, due to its low friction and high hardness which offer a high protection against abrasive wear in tribological applications. However, DLC coatings also present some undesirable properties which prevent their wider use in industry, such high internal stress levels developed during the energetic deposition process, resulting in high strain on the interface with substrate and finally low adhesion strength. In addition a common limitation of DLC coatings is their low thermal stability, since their sp^3-sp^2 structure undergoes a graphitization process at high temperatures, deteriorating both hardness and wear behaviour [1-4]. One common strategy to overcome the high stress is to dope the DLC coating with metal species, mainly carbide former elements such as Ti, W, Nb, Mo and Zr [5-8]. By adjusting the concentration of these metals into the carbon matrix, it would be possible to form carbide nanoclusters that could restrict deformation and crack propagation. However, the formation of Me-C bonding would reduce the availability of free carbon needed to generate lubricious graphitic tribolayers that would improve friction and wear resistance [9]. Metals of non-carbide formers such as Ag and Al have also been studied as doping alternatives for DLC coatings [10, 11]. These metals would promote the formation of ductile phases that support plastic deformation of the coating, thus improving toughness and releasing internal stresses. However, the stress relaxation usually destabilizes the sp^3 bonding structure in the DLC matrix, which would cause a decrease on the coating hardness [12, 13].

Conventional magnetron sputtering techniques have been primarily used for the synthesis of metal-containing DLC coatings, often leading to low-density microstructures and poor mechanical properties because of the rather low degree of ionization for metal and gas species [14, 15]. As compared to conventional magnetron sputtering technique, high power impulse

magnetron sputtering (HiPIMS) can provide larger fractions of ionized atoms in argon-metal discharges combined with high plasma densities (10^{19} m^{-3}) [16]. A highly ionized plasma would enable to have a higher ion bombardment of the growing film, resulting in denser coatings with improved mechanical properties [17]. However, there are studies showing that even in the standard HiPIMS process, the ionization probability of sputtered carbon is still insufficient to achieve optimum DLC properties [18]. Therefore, new approaches such as the codeposition with different techniques, DC-pulsed for carbon and HiPIMS for metal doping, might provide solutions to the existing ionization problems.

By synthetizing metal-doped DLC with the aid of highly ionized HiPIMS metal plasma discharges, we have aimed at maintaining the high hardness and the low coefficient of friction values of the un-doped DLC coatings, while reducing their internal stresses and increasing their high temperature tribomechanical behaviour. Among all candidates DLC-doping metals we have chosen Cr as it can provide high resistance to wear at high temperatures by promoting the formation of stable tribolayers at the point of contact [19, 20]. Moreover, due to its small size and toughness, it could also improve the coating load bearing ability due to a better distribution of the supported load during operation and in doing so it could reduce the internal compressive stress. Cr-doped DLC coatings has been previously deposited with PVD techniques such as cathodic arc evaporation [21], magnetron sputtering [20] and linear ion beam technique [22, 23], showing in all cases the graphitization of the carbon structure when Cr was introduced into the carbon matrix. In this work, we focused on the potential of HiPIMS technique to synthetize Cr-doped DLC with enhanced properties, as Cr-HiPIMS plasma discharges have the potential to produce metal ions with energies up to 100 eV and the ionization degree can be up to 90% [24]. In our previous work, we have also shown the benefits of HiPIMS to deposit Cr interlayers with improved DLC adhesion on industrially relevant steel substrates by accommodating the plastic deformation [25]. Cr-doped DLC coatings were deposited by co-sputtering, using a HiPIMS unit for Cr deposition and a DC-

pulsed magnetron sputtering unit for deposition of DLC. Coatings with different Cr doping contents were obtained by varying the HiPIMS target current and frequency. The influence of co-sputtering process parameters on the microstructure, mechanical and tribological properties of the deposited coatings was evaluated at different temperatures.

2. Experimental methods

2.1. Deposition method

Coatings were deposited in a custom-made batch type coating system designed and manufactured by Nano4Energy S.L. This system has a volume of 0.8 m^3 and is equipped with two Gencoa SH100400 cathodes using rectangular graphite and WC:Co (6% wt. Co) targets with an area of 400 cm^2. In addition, a circular N4E 2" cathode using a chromium target with an area of 20 cm^2 was also used for the Cr-doping control. A sketch of the experimental setup is shown in Fig. 1.

Coatings were deposited on mirror electropolished (average roughness $R_a \approx 5$ nm) stainless steel (SS304) with a size of 40x40 mm^2 and on commercial (100) silicon substrates with a size of 15x15 mm^2. Prior to the deposition of the coatings, substrates were cleaned using a sequence of ultrasonic washing with alkaline detergents, rinsing with de-ionized water, cleaning with isopropanol and air-drying.

Optimum coating-substrate adhesion was achieved by the following steps: 1) argon etching using a DC-pulsed substrate bias voltage of -500 V and a frequency of 150 kHz; 2) HiPIMS metal ion etching pretreatment with Cr ions using a target voltage of 1100 V, a substrate bias voltage of 750 V, a pulsing time of 100 µs and a frequency of 100 Hz; and 3) deposition of a WC interlayer in the DC-pulsed mode with a power density of 1.5 W/cm^2, a peak voltage of 1050 V, a pulse width of 2.7 µs and a frequency of 150 kHz . More details about the engineered interface for adhesion enhancement are provided in ref. [25]. The Cr-doped DLC coatings were deposited using a combination of HiPIMS and DC-pulsed magnetron sputtering

technique at a working pressure of 0.65 Pa in a non-reactive Ar atmosphere. The graphite target was connected to an Enerpulse EN10 DC-Pulsed power supply operating at a power density of 1.5 W/cm^2, a peak voltage of 1200 V, a pulse width of 2.7 μs and a frequency rate of 150 kHz. The chromium target was connected to a hip-V 6 kW power supply operating under HiPIMS mode. The power applied to the Cr magnetron as well as, the pulsing frequency was varied to obtain different chemical compositions and microstructures. Further details on Cr deposition conditions are given in section 3.1.

For plasma characterization, voltage and current waveforms of the pulses applied on the Cr target were measured using a high voltage differential probe (100:1 attenuation) and a PEM Rogowski probe sensor connected to a Tektronix TPS 2012 oscilloscope were used.

2.2. Elemental composition and structural characterization

The surface and thickness of the films were investigated by scanning electron microscopy (SEM) using a FEI Verios 460 Field Emission XHR-SEM. Deposition rates were calculated by dividing the thickness of the coatings as estimated by cross-sectional SEM images by the deposition time. The residual stress (σ_f) was measured using the substrate curvature method based on the Stoney´s equation [26]:

$$\sigma_s = \frac{E_s \cdot h_s^2}{6h_f(1-\vartheta_s)}\left(\frac{1}{R}-\frac{1}{R_0}\right)$$

where E_s and υ_S, are the Young's modulus and Poisson ratio of the stainless steel substrate, taken as 200 GPa and 0.3 respectively. The thickness of the substrate, h_S, was 200 μm, with an initial radius of curvature, R_0, of 500 m, while the coating thickness h_f, ranged from 1000 to 1500 nm. The radius of curvature of the coated substrate, R, was measured with a Leica DCM 3D confocal profilometer.

X-ray photoelectron spectroscopy (XPS) was used to evaluate the Cr content of the coatings and the potential formation of carbides. XPS spectra were measured using a VG ESCALAB 210 instrument, which was upgraded with a SPECS Phoibos 100 DLD hemispherical electron

energy analyser. Non-monochromatic Al Kα radiation (1486.6 eV) was used as X-ray excitation source. The measurements were performed in constant analyser energy mode with a 35eV pass energy for high resolution spectra of the detected elements. Samples were previously cleaned using Ar^+ ion bombardment at a pressure in the order of 10^{-6} mbar (2 keV; 15-20 μA) for 10 min. Quantification was accomplished by determining the elemental areas of C 1s, O 1s and Cr 2p peaks, following a Shirley background subtraction and accounting for the relative sensitivities of the elements using Scofield cross-sections. The fitting analysis was then performed by a least squares fit of the C 1s of the films to estimate the relative amount of the different carbon bonds (carbides, C-C, C=O and carbonates) in agreement with previous works [27].

Rutherford backscattering spectroscopy (RBS) was used to verify the elemental composition of the films. Measurements were performed at the Centro Nacional de Aceleradores (CNA) using a He^+ beam at the energy of 4250 KeV. At this energy, the cross section for Cr is "Rutherford" but that for C is "Non-Rutherford" [28] which would allow to have a better accuracy in the determination of the C content in the films. The backscattered ions were detected by a standard Si-barrier detector located at an angle of 165º to the beam direction. The elemental composition of the films was determined by comparing measured and simulated spectra. For the simulations the commercial computer code SIMNRA was used [29].

Raman characterization was performed in order to evaluate the structural properties of DLC films. Raman spectra were recorded using a Renishaw inVia micro-Raman spectrometer. An argon ion laser with a line of 532 nm was focused on the surface of the coatings with a power of 10 mW. The measurement time was 10 s and spectra were accumulated 10 times in order to reduce the noise level. The obtained Raman spectrum was curve-fitted using two Gaussian

functions, peaking at disordered (D-band) and graphite (G-band) modes. The relative intensity ratio of the D and G bands (I_D/I_G) was obtained from the ratio of peak heights.

Transmission electron microscopy (TEM) and scanning transmission electron microscopy - high angle annular dark field (STEM-HAADF) images were obtained in a FEI Tecnai field emission gun scanning transmission electron microscope (STEM-FEG), mod. G2F30, working at 300 kV. Cross-sectional specimens for TEM analysis were produced by ion milling using a FEI Helios Nanolab 600i dual beam FIB-FEGSEM.

Electron energy-loss spectroscopy (EELS) spectra were recorded with a Gatan Imaging Filter (GIF, QUAMTUM SE model) attached to the microscope. The carbon core–loss spectra were recorded and the background and the multiple plural scattering were removed using a digital micrograph software. After that, each spectrum was normalized by dividing the whole spectrum by the edge intensity at 294 eV. The spectrum exhibited two characteristic features: the 1s→π* transition at ~284 eV and the 1s→σ* transition occurring at ~291 eV. The sp^2 fraction was calculated using the Ferrari's formula [30]:

$$sp^2 = \frac{\left[\frac{area(\pi^*)}{area(\pi^*+\sigma^*)}\right]_{sample}}{\left[\frac{area(\pi^*)}{area(\pi^*+\sigma^*)}\right]_{100\%\ sp^2 reference}}$$

The used 100% sp^2 reference was a polycrystalline graphite sample deposited onto a holey carbon grid and the spectra were measured at magic angle conditions, at which the carbon signal would be independent of the sample orientation (TEM mode and a spectrometer collection angle of 1 mrad). The area of π* and σ* were obtained by integrating the intensity over a 4 eV window (282-286 eV) and 10 eV window (288-298 eV) respectively following the two-window method described by S. Urbonaite [31]. Several measurements were done for each sample in order to obtain a mean % sp^2 value. This value was corrected to take into account the increase in the sp^2 fraction due to FIB damage during specimen preparation [32].

2.3. Mechanical properties

Nanoindentation measurements were performed using a Triboindenter TI950 from Hysitron. For high temperature nanoindentation testing, a hot stage (Hysitron xSol) and a Berkovich diamond indenter fitted to a special long insulating shaft were used. In this configuration, the sample is placed between two resistive heating elements in order to eliminate temperature gradients across the sample thickness. Dry air and argon around the tip and sample surface were used to purge the testing area to prevent heated gases reaching the transducer and reduce oxidation. Once the sample reached the selected temperature (100, 200, 250, 300, 350, 400, 425ºC) and was stable at the target temperature to within ± 0.1 °C, the tip was placed at about 100 μm from the sample surface for 10-15 minutes, to ensure passive heating of the tip before the start of the test and minimize thermal drift.

In order to obtain reproducible and accurate results at least six indents were performed at different positions. The indentations were performed under load control, using loading, holding and unloading times of 5, 5 and 2 s respectively, and peak loads of 3 and 7 mN. Reduced elastic modulus (E_r) and hardness were determined from the recorded load-displacement curves using the Oliver & Pharr method [33].

2.4. Tribological properties

A high temperature pin-on-disk tribometer was used to measure the coefficient of friction (COF) and the volumetric wear of the coatings at a speed of 0.1 m/s and a normal load of 5 N for up to 5000 revolutions. Sliding tests were carried out under environmental conditions at different temperatures (RT, 100, 125, 150, 175 and 200ºC). The testing counterparts were Al_2O_3 balls with a diameter of 6 mm. Two sliding tests were performed at each temperature and a new counterface was used for each test. Each friction curve was characterized by the

value of COF once the steady state stage was reached. The wear of the tested Cr-DLC coatings was calculated from the volume of the material removed, which was measured from the cross-sectional area of the wear track at four different locations along the circular sliding track. A Leica DCM3D optical profilometer was used for this purpose. The reported volumetric wear rates were the mean values obtained from tests run for 5000 revolutions at each temperature.

The wear tracks generated on the Cr-DLC coatings and the transfer layers formed on the Al_2O_3 counterface surfaces during the sliding contact were examined by Raman spectroscopy and SEM with an energy dispersive spectroscopy (EDS) detection system. Some tribological tests were interrupted during the running-in period in order to carry out Raman analysis at this initial stage.

3. Results and discussion

3.1. Enhanced ionization of chromium by HiPIMS codeposition

Coating deposition has been carried out under the voltage-control mode. The main deposition parameters, together with the Cr content, the deposition rate and the residual stress of the coatings are summarized in Table 1. The Cr-HiPIMS current waveform obtained during Cr-doped DLC coatings deposition shows the same overall trend for all the studied samples. An initial current peak of several amperes was reached after approximately 10 μs followed by a continuous current decay. The decrease in current after the initial peak is a common observation in non-reactive HiPIMS Cr deposition due to the displacement of working gas ions by metallic ions of the sputtered Cr target. According to literature, in this phase highly energetic Cr ions are observed [24].

The amplitude of the current peak during Cr-HiPIMS discharge at a fixed target voltage of 1100V as a function of the working frequency is shown in Fig. 2. At frequencies higher than

50 Hz, current peak values remain constant. However, at frequencies lower than 50 Hz and a fixed target voltage of 1100 V, a substantial increase in the current peak intensity is observed with decreasing working frequency. The origin of this effect might be associated to the carbon contamination on the Cr target surface. At frequencies <50 Hz, the HiPIMS pulse applied to the Cr target is mostly off and during this time thin carbon layers are formed on the surface of the Cr target, generating a light (C)-heavy (Cr) elements layered structure, which could amplify the sputter yield. Such an enhancement has been previously reported during the sputtering of inhomogeneous targets, as the one we are dealing with, under certain deposition conditions [34, 35, 36]. Nevertheless, as stated by Anders *et al.*, the very large differences may not only be due to the different sputter yields but also to the generation and trapping of secondary electrons [37]. Thus, in our case it may be that the C-Cr layered structure present in the target due to contamination allowed igniting the discharge with a high current density. ~~and the secondary electron emission by the so-called sputter yield amplification (SYA) effect. According to this, heavier atoms in the target would behave as recoil centres, which would reflect the lighter atoms towards the target surface. This effect has been previously seen for carbon doped with Pt and has been known to increase the deposition rate of carbon-based coatings [36]. The low atomic mass of carbon favours the selection of suitable metals to achieve this effect, such as: Nb, W or, as in this case, Cr. It is worth noting that usually the increase in sputter yield is affected by the carbon target contaminated by a metal dopant atoms during the carbon plasma discharge. However, in our case, the contamination of the Cr target by the deposition of C layers is the origin of the SYA effect.~~ The C-Cr layered structure present in the target due to contamination leads to the ignition of the discharge with a high current density. Later, the current remained high due to the large secondary electron emission obtained during the first stage of the discharge.

There are other contributing factors to explain the reduced Cr content in DLC:Cr_1 such as

backscattering effects. Due to the commonly high ionization rate encountered in HiPIMS discharges, some of the ionized Cr target atoms are attracted back to the target surface [37, 38], thus reducing the incorporation of Cr into the coating structure. Further investigations are being carried out in order to clarify the role of backscattering effects and to understand the operation principle that enables current density amplification.

As shown in Table 1, the Cr content in the coatings increases with rising Cr target power. The highest Cr content (20 at. %) is observed for the DLC:Cr_3 coating deposited at 100 W. However, not only the Cr target power plays a role in the incorporation of Cr but also the deposition frequency. Indeed, we observed that the Cr content for samples deposited at the same target power (25 W), increased from 3 to 9 at. % when changing the deposition frequency from 15 Hz to 50 Hz corresponding to the DLC:Cr_1 and DLC:Cr_2 samples, respectively. This was so, because when working at low frequencies, the carbon contamination produced when HiPIMS pulses are off played a significant role on reducing the amount of Cr incorporated to the DLC coating.

As expected, deposition rates increased with target power, while for the same power (25 W), the lower the working frequency, the lower the deposition rate (sample DLC:Cr_1) as seen in Table 1. The decrease in the deposition rate with diminishing the frequency is related to the higher plasma currents obtained during the synthesis. This led to larger metal ion energies during the coating deposition and increased bombardment of the growing coating surface, enhancing the peening effect.

All the Cr-DLC films exhibit a residual stress lower than that of the undoped DLC sample. There are two main factors that explain the reduction of the residual stress level when doping with Cr. Firstly, the Cr ion bombardment increases adatom mobility during the coating growth which contributes to the relaxation of the residual stress of the film [39], and secondly, the metal incorporation reduces the directionality of the C-C bond and promotes the generation of Me-C bonds in such a way that the distortion of the C-C bond structure reduces

the compressive stress level as described in ref. 40 and 41.

3.2. Microstructural characterization

Raman analysis was performed in order to obtain information on the nature of carbon bonding structure. The Raman spectra presented in Fig. 3 exhibited an asymmetric G band centred at ~1560 cm^{-1} and an overlapping broader D band centred at ~1360 cm^{-1}. These two characteristic Raman active bands are usually observed in amorphous carbon films due to the sp^2 sites since its Raman scattering cross section is 50 times larger than that of the sp^3 sites [42]. The G band would correspond to the symmetric E_{2g} C–C stretching mode in all sp^2 sites (both chains and rings), while the D band would be a breathing mode of A_{1g} symmetry involving only those sp^2 sites in rings [43]. A multiple Gaussian fit of the spectra into the G and D-peaks would enable the analysis of the structural differences between coatings. Peak fitting was performed in the spectral range 800-2000 cm^{-1} using Gaussian functions, as these functions give a better fit for disordered amorphous carbon films than Lorentzian functions.

The calculated I_D/I_G ratios and G position suggest that the presented coatings are in a stage 2 (a-C) in the transition to stage 3 (ta-C) of the Ferrari´s three stage model for a 514 nm excitation wavelength [44].

It is worth noting the reduction in the intensity of the Raman signal when introducing even low amounts of Cr in the amorphous carbon matrix. This effect has also been observed in previous studies when doping DLC with other metals such as V, Zr and W [45]. This is due to the reduction of the light absorption capability of the DLC coatings when introducing metal dopants. Such a reduction makes that a higher proportion of the laser beam is reflected from the surface, which cannot generate a Raman signal reaching the detector.

An important observation from Fig. 3 is that the Cr addition generally would increase the

I_D/I_G ratio, which would be in accordance with previously reported studies for samples doped with Ti, V, Zr, W deposited by magnetron sputtering [45]. In our particular case, the I_D/I_G ratio increased from 0.43 (DLC) to 0.62 (DLC:Cr_1), while for the highest Cr content (DLC:Cr_3), the I_D/I_G ratio increased to 1.32. According to literature, the I_D/I_G ratio is proportional to the number and clustering of rings and is especially sensitive to the number of ordered rings in the stage 2 to stage 3 transition [44]. A decrease in the intensity of the D-peak would then be associated to a gradual change in sp^2 sites from rings to chains and to the presence of sp^2 dimers embedded in the sp^3 matrix. The π states become increasingly localized on olefinic chains. Olefinic bonds are shorter than aromatic bonds and have higher vibration frequencies which turns in I_D/I_G ratios close to zero. This effect is more pronounced when higher sp^3 contents are present in the carbon structure [44].

Fig. 3 also shows that the G peak position moves to higher wavenumbers with increasing Cr content. For DLC, the G-peak position is centred at 1541 cm^{-1}, for DLC:Cr_1 the position is slightly shifted towards lower values (1538 cm^{-1}), while for DLC:Cr_2 and DLC: Cr_3, the position is shifted towards more positive values (1551 cm^{-1} and 1563 cm^{-1} respectively). The G-peak position is also altered due to the change of sp^2 configuration from rings to olefinic groups. The G skewness tends to decrease and moves towards lower wavelengths due to the more localized sp^2 chains [46]. Therefore, the reduction in I_D/I_G ratio together with the shift in the position of the G-peak towards lower wavenumbers with decreasing Cr content are indicative of an increase in the sp^3 fraction. Further information on the sp^3 content of deposited coatings was obtained from TEM and EELS analyses, which can also provide evidence of the potential presence of carbides.

Fig. 4 shows representative HRTEM and HAADF-STEM micrographs for the DLC, DLC:Cr_1 and DLC:Cr_2 samples. The DLC and DLC:Cr_1 present a homogeneous

microstructure characteristic of an amorphous material. However, DLC:Cr_2 exhibits a nanocomposite microstructure, where bright grains of 2-5 nm size, which corresponds to a heavier composition (higher Z) in a HAADF image, are embedded in a matrix of darker contrast.

Fig. 5 shows representative EELS spectra for the same three coatings. In the case of DLC:Cr_2, the EELS spectra was measured in two different areas: within the carbon matrix (M) and within a grain structure (G). Also, a graphite and Cr_3C_2 spectra are presented as references for comparative purposes. The fine structure of the graphite spectrum presents two characteristic peaks, which correspond to the $1s\rightarrow\pi^*$ and $1s\rightarrow\sigma^*$ transitions occurring at ~ 284 and 291 eV respectively, while the chromium carbide presents a wider peak around 283 eV and a shoulder at 294 eV. The spectra of the DLC and DLC:Cr show similar fine-structures: A peak at 284 eV (π^* peak) and a plateau between 290 and 300 eV. The intensity of π^* peak at 292 eV differs from sample to sample highlighting the variations of the sp^3 fraction [47, 48].

The measured spectra for DLC, DLC:Cr_1 and DLC:Cr_2 (M) show very similar features, which is reflected in the estimated sp^3 contents of 27±3 %, 28±5 % and 24±3 % for DLC, DLC:Cr_1 and DLC:Cr_2(M), respectively (see table 3). The absence of significant differences in the sp^3 values for the DLC:Cr_1 and the DLC:Cr_2 (M) in comparison with the undoped DLC sample indicate that the carbon atoms maintain their structural coordination in the network at these low levels of Cr incorporation (≤ 9at.%). The spectra measured in the grain, DLC:Cr_2(G), presents a higher and wider π^* peak, a decrease in the intensity of σ^* peak and an increase in the intensity at energies above 294 eV. These changes can be attributed to the presence of C-Cr bonds. The spectrum can be therefore considered as a combination of DLC and chromium carbide phases. Thus, the brightest grains observed in the

Fig. 4 of DLC:Cr_2 must correspond to chromium carbide grains formed inside the DLC matrix.

In Fig. 5b, the Cr-$L_{2,3}$ edge EELS spectra for DLC:Cr_2 is compared with those for metallic chromium and Cr_3C_2 references samples. Despite the noisy spectra for DLC:Cr_2, a difference in the ratio of the lines (L_3/ L_2) can be observed. An intermediate value is obtained for DLC:Cr_2 indicating, in addition to the formation of chromium carbide, the presence of some metallic chromium Cr^0 atoms dispersed in the DLC matrix. For DLC:Cr_1 it was not possible to measure any Cr $L_{2,3}$ signal due to the high dispersion and low Cr content. But taking into account the above results for DLC:Cr_2 and the previous results for low Cr doped-DLC [49], the chromium in the DLC:Cr_1 sample must be distributed as metallic chromium throughout the carbon network. No results on sp^3 contents are presented for the DLC:Cr_2(G) and for the DLC:Cr_3 because higher Cr doping contents led to broad overlapped peaks, which resulted in a much more complex interpretation on the nature of the carbon structure [50, 51, 52].

Further investigations on the formation of carbides was obtained from XPS measurements of the C1s peaks. C1s spectrum for the DLC and Cr-DLC coatings are shown in Fig. 6. The C1s spectrum was deconvoluted into four components centred at 283.3 eV, 284.8 eV, 286.5 eV and 288.4 eV, which correspond to C-Cr bonds, C-C bonds, C-O bonds and C=O bonds, respectively. The C-O and C=O signals are rather low and can be associated to oxygen adsorbed on the surface. There was no C-Cr peak present for DLC:Cr_1, which could be expected since there was not enough Cr content for carbide formation. The intensity of the C-Cr peak increased with Cr content, but still remained very low compared to the most intense peak arising from C-C bonds.

No crystalline chromium carbide phase could be found for samples with low Cr content. In

spite of this, the catalytic activity during surface diffusion of the metal atoms could still have been responsible for the promotion of clustering of sp^2 hybridized carbon in to aromatic rings [45]. These results would indicate that for sample with low Cr content (3 at.%), deposited under the conditions shown in table 1, the use of highly energetic plasma discharges may facilitate the introduction of Cr into the carbon network while maintaining the original carbon structure.

3.3. Mechanical properties

Fig. 7 shows load-depth curves for DLC and Cr-DLC coatings when indentations were performed using a load of 7 mN. The maximum penetration depth was ≈ 145 nm for the DLC:Cr_3, and < 100 nm for the DLC sample. No substrate effect was found as maximum indentation depths were ≤ 10% of total film thickness and similar results were found using smaller loads. The area inside the curves for the DLC and the DLC:Cr_1 samples was smaller than for the other two which would indicate a higher elastic recovery of the coatings upon unloading as less energy would dissipate during deformation.

Table 2 shows the hardness (H) and reduced elastic modulus (E_r) of the DLC and Cr-doped DLC films. DLC (31.4 GPa) and DLC:Cr_1 (29.2 GPa) samples exhibit hardness values that are almost twice those found for DLC:Cr_2 (17.6 GPa) and DLC:Cr_3 (15.4 GPa). Since, tthe hardness and elastic modulus of hydrogen-free amorphous carbon films have been known to correlate with the carbon bonding configuration [52]. The decrease in hardness and elastic modulus of the coatings could be attributed to the formation of aromatic bonds induced by less energetic deposition processes due to increased Cr doping contents. This is in accordance with the Raman and EELS results presented earlier. Also, these results would be in agreement with those reported for Cr-DLC [19, 20] where the introduction of Cr led to the destabilization of the carbon structure and the subsequent hardness decay.

The H/E ratio for all studied samples is depicted in table 2. The H/E ratio for DLC and DLC:Cr_1 was ≈ 0.125, higher than that found for DLC:Cr_2 and DLC:Cr_3 samples (H/E=0.106). As this ratio is related to the resistance to elastic strain failure [53], these results would indicate that DLC and DLC:Cr_1 would be able to better accommodate substrate deflections under higher loads.

The H^3/E^2 ratio decreased with increasing Cr content from DLC ($H^3/E^2 = 0.516$) to DLC:Cr_3 ($H^3/E^2 = 0.176$). Since this ratio is an indicator of the ability of the material to dissipate energy under load due to plastic deformation [53, 54], these results would indicate that the addition of Cr would enable the coatings to better accommodate deformation without cracking.

Fig. 8 shows the evolution of mechanical properties with increasing testing temperature. Hardness values exhibit a slight steady drop for all four samples as the temperature is raised from RT to 300°C. Above 300°C, a sharp reduction in hardness is observed for DLC:Cr_3, while DLC:Cr_2 experiences a significant drop in hardness at T > 350°C. For DLC and DLC:Cr_1 samples, the high hardness values are maintained at higher temperatures (T > 400°C). The elastic modulus followed a similar trend, with modulus values remaining nearly constant up to 300°C, after the initial drop observed between RT and 100°C for DLC and DLC:Cr_1 samples. The modulus values started to drop significantly at T > 400°C for DLC and DLC:Cr_1, while the modulus drop started earlier and it was more pronounced for DLC:Cr_2 (T > 350°C) and for DLC:Cr_3 (T > 300°C). In principle, the hardness reduction during early stages of heating may be assigned to some degree of stress relaxation due to clustering of sp^2 sites in the films, as moderate temperatures up to 200 °C would not be expected to have a noticeable effect on the fraction of sp^3 to sp^2 bonding [55].

Raman spectroscopy was used in order to evaluate the possible temperature-induced modifications on the sp^2 carbon film structure. Fig. 9 shows the Raman spectra of the

different coatings after nanoindentation tests at 400°C. After annealing at 400°C, the I_D/I_G ratio rises and the G band is gradually transformed into a sharp G peak corresponding to crystalline bulk graphite [56]. The D-band alterations are difficult to interpret as they can correspond to a superposition of different carbon structures that may undergo different modifications [56, 57, 58]. Prior to annealing, the D-band is rather broad which corresponds to sp^2 clusters of different sizes. During annealing, the D-band is getting sharper with increasing temperature, as observed in previous studies [59]. A narrower breathing mode has been associated to the formation of sp^2 clusters of similar size and shape [58].

Table 3 shows the values of the I_D/I_G ratio before and after the high temperature testing at 400°C. The largest increase in the I_D/I_G ratio occurred for the samples with the highest Cr content (DLC:Cr_2 and DLC:Cr_3). Also, the shift of the G peak position towards higher wavenumbers was more notorious for these samples. As previously explained in section 3.2, the increase in the I_D/I_G ratio can be associated with the conversion of sp^3 bonds to sp^2 and the subsequent clustering of sp^2 sites [12]. This clustering would lead to a reduction of the compressive stress, which could be seen by the shift of the G peak position to higher wavenumbers [44].

Top view SEM images of the DLC sample after annealing at 450ºC (not shown) evidence that annealing at this temperature led to an increase in the surface roughness and to the appearance of some blisters and delaminated spots. These results would indicate that the graphitization process associated with the rise in temperature would probably start in the near surface atoms before reaching the bulk of the films. The appearance of small blisters could be related to the higher degree of sp^2 clustering at high temperature. These defects generated by the surface relaxation leads to higher surface roughness, especially for the samples with large sp^2 content as well as, to the emergence of delamination spots [60].

3.4. Tribological properties

Fig. 10 shows the COF measured at room temperature (RT) as a function of the number of cycles for the DLC and Cr-doped DLC coatings. At RT, the COF was relatively stable showing a distinguishable running-in period of less than 350 cycles, being the running-in time longer and the COF higher as the Cr content is increased. Raman analysis examined on wear tracks (not shown) revealed the presence of broad bands at 300 and 800 cm^{-1} could be attributable to chromium oxides during the running-in period for Cr-doped DLC samples that could explain the transient increase in friction. After this initial period, the COF decreased due to the formation of graphitic transfer layers, reaching a steady state with constant values that are maintained for the rest of the test. Low average values of COF were obtained during this stage: 0.16 for DLC, 0.12 for DLC:Cr_1, 0.12 for DLC:Cr_2 and 0.14 for DLC:Cr_3.

The evolution of steady state COF and wear rate values with temperature for all four samples is plotted in Figs. 11a and 11b, respectively. In general, the COF values were low at moderate temperatures, up to 150ºC. The decrease observed in the COF with increasing temperature, in this temperature range, is related to the advance of the graphitization process with temperature. The graphitization process would weaken the shear strength at the surface and it would generate a transfer carbon tribo-layer at the sliding contact that reduces friction [2]. The temperature range where graphitization occurred during tribological testing was much lower than the one observed during mechanical testing. Fig. 12a shows the micro-Raman spectra obtained from the wear tracks of DLC:Cr_1 at RT, 100, 150 and 200 ºC. The rise of the D-band peak intensity in the Raman spectra of the worn track surfaces would indicate an increase in sp^2 bonds at high temperatures. These changes in the bonding structure are attributed to sliding and temperature induced graphitization [61]. Theories on graphitization of DLC, such as that proposed by Haque *et al.* [62], suggest that the high contact pressure exerted by debris generated during wear between sliding contacts facilitates the sp^3 to sp^2 transformation at temperatures lower than those found in quasi-static tests such as nanoindentation. Fig. 12b shows the Raman spectra analysed within the wear track of the

samples after pin-on-disk testing at 150°C. The I_D/I_G is enhanced with higher Cr contents, which would indicate that the graphitization process would be enhanced when higher levels of sp^2 sites clusters are initially present in the structure of the coatings.

Graphitization could be therefore considered the main factor controlling the wear behaviour. Fig. 11b shows wear rates for all samples during tests performed at RT, 100, 125, 150, 175 and 200°C. DLC and DLC:Cr_1 exhibit significantly lower wear rates as compared with DLC:Cr_2 and DLC:Cr_3. A large increase in wear rates was observed for the DLC:Cr_2 and DLC:Cr_3 samples at T > 150°C, which would be associated with the extended graphitization process taking place in this temperature range.

The severe wear was particularly visible in the scanning electron microscopy images shown in Fig. 13c and for the DLC:Cr_2 and DLC:Cr_3 samples, which were taken after tests performed at 175°C. It is also worth noting the presence of delamination spots along the wear track on the undoped DLC coating (Fig. 13a). This brittle failure mode would minimize the amount of elastic energy stored by the large compressive stress ahead of the moving ball. The introduction of Cr into the DLC structure reduces the accumulated compressive stress within the film, preventing early adhesive failure (Fig. 13b). Small additions of Cr, as is the case for coating DLC:Cr_(containing 3 at.% Cr) would confer optimum ductility to the loaded coating, making it more capable of distributing the load during the sliding test, therefore exhibiting the best sliding behaviour, even at high temperatures.

4. Conclusions

Cr-doped DLC coatings with different Cr content from 0 at. % up to 20 at. % were co-deposited using a HiPIMS technique under highly energetic conditions. The carbon-based structure (DLC) was obtained using DC-pulsed mode, while the addition of Cr was controlled by the HiPIMS discharge by adjusting the pulse frequency and power. For the same power, very high current discharges were obtained at low working frequencies (down to 15 Hz) on

the Cr target~~, which was related to the SYA effect caused by carbon contamination on the Cr target~~.

Under these deposition parameters, low levels of Cr (up to 3 at. %) are incorporated into the DLC carbon structure without major disruption of the C-C sp^3 network (as evidenced by Raman and EELS) and without any significant effect on the mechanical properties. Moreover, the internal stresses of the coatings are reduced and delamination behaviour is improved as coatings exhibited a more plastic behaviour than the undoped DLC preventing early brittle failure.

The graphitization process is delayed at high temperatures, which is associated to the chain-like carbon structure so that the friction mechanism is dominated by the formation of graphitic tribolayers, a process facilitated by the addition of small amounts of Cr (up to 3 at. %) into the carbon structure.

In summary, we have tuned the deposition parameters and Cr content to achieve a Cr-doped DLC (3 at. % Cr) coating with lower intrinsic stress, less brittle behaviour, same mechanical and tribological properties and, better high temperature frictional behaviour than the undoped DLC. These findings would bring great benefits for novel high-temperature and high-load tribological applications.

Acknowledgments

The research leading to these results has received funding from Madrid region under programme S2013/MIT-2775, DIMMAT project. Financial support from MINECO under projects (RADIAFUS IV ENE2015-70300-C3-3-R, MAT2014-59772-C2-1-P, MAT2015-69035-REDC FUNCOAT+), Leverhulme International Network Grant (CARBTRIB) and EUROfusion Consortium under project AWP15-ENR-01/CEA-02 are also acknowledged.

Notes

References

[1] Y. Liu et al., *An investigation of the relationship between graphitization and frictional behaviour of DLC coatings*, Surface and Coatings Technology, 86-87 (1996) 564-568

[2] Y. Liu et al., *Influence of environmental parameters on the frictional behaviour of DLC coatings*, Surface and Coatings Technology, 94-95 (1997) 463-468

[3] W.J. Yang et al., *Thermal stability evaluation of diamond-like nanocomposite coatings, Thin Solid Films*, 434 (2003) 49-54

[4] H. Ronkainen, K. Holmberg, *Environmental and Thermal Effects on the Tribological Performance of DLC coatings*, Tribology of Diamond-Like Carbon Films, 155-200 (2008)

[5] J.C. Sánchez-López, A. Fernández, *Doping and Alloying Effects on DLC coatings*, Tribology of Diamond-Like Carbon Films, 311-338 (2008)

[6] A.A. Voevodin et al., *Design a Ti/TiC/DLC functionally gradient coating based on studies of structural transitions in Ti-C thin films*, Thin Solid Films, 1-2 (1997) 107-115

[7] T. Vitu et al., *Sliding properties of Zr-DLC coatings: The effect of tribolayer formation*, Surface and Coatings Technology, 258 (2014) 734-745

[8] C. Corbella et al., *Preparation of metal (W, Mo, Nb, Ti) containing aC:H films by reactive magnetron sputtering*, Surface and Coatings Technology, 177-178 (2004) 409-414

[9] T.W. Scharf, I.L. Singer, *Role of the transfer film on the friction and wear of metal carbide reinforced amorphous carbon coatings during run-in*,Tribology Letters, 36 (2009) 43-53

[10] N.K. Manninen et al., *Influence of Ag content on mechanical and tribological behavior of DLC coatings*, Surface and Coatings Technology 232 (2013) 440-446

[11] S. Zhou et al., *A simple solution-immersion process for the fabrication of superhydrophobic cupric stearate surface with easy repairable property*, Applied Surface Science 257 (2011) 6971-6979

[12] R. Kalish, Y. Lifshitz, *Thermal stability and relaxation in diamond-like carbon. A*

Raman study of films with different sp^3 fractions (ta-C to a-C), Applied Physics Letters, 74 (1999) 2936

[13] A.C. Ferrari et al., *Determination of bonding in diamond-like carbon by Raman spectroscopy*, Diamond and Related Materials 11 (2002) 994-999

[14] U. Helmersson et al., *Ionized physical vapor deposition (IPVD): A review of technology and applications*, Thin Solid Films 513 (2006) 1-24

[15] J.A. Santiago et al., *The influence of positive pulses on HiPIMS deposition of hard DLC coatings*, Surface and Coatings Technology 358 (2019) 43-49

[16] D. Lundin et al., *Anomalous electron transport in high power impulse magnetron sputtering*, Plasma Sources Sci. Technol. 17 (2008) 025007

[17] K. Sarakinos et al., *High power pulsed magnetron sputtering: A review on scientific and engineering state of the art*, Surface and Coatings Technology 204 (2010) 1661-1684

[18] A. Aijaz et al., *A strategy for increased carbon ionization in magnetron sputtering discharges*, Diamond & Related Materials 23 (2012) 1-4

[19] V. Singh et al., *Cr-diamondlike carbon nanocomposite films: synthesis, characterization and properties*, Thin Solid Films 489 (2005) 150-158

[20] C.W. Zou et al., *Effects on Cr concentrations on the microstructure, hardness and temperature-dependent tribological properties of Cr-DLC coatings*, Applied Surface Science 286 (2013) 137-141

[21] M.C. Chiu et al., *Thermal stability of Cr-doped diamond-like carbon films synthesized by cathodic arc evaporation*, Thin Solid Films 476 (2005) 258 – 263

[22] W. Dai et al., *Synthesis, characterization and properties of the DLC films with low Cr concentration doping by a hybrid linear ion beam system*, Surface and Coatings Technology 205 (2011) 2882-2886

[23] W. Dai et al., *Effect of bias voltage on growth property of Cr-DLC film prepared by linear ion beam deposition technique*, Vacuum 85 (2010) 231-235

[24] A. Hecimovic et al., *Time evolution of ion energies in HIpIMS of chromium plasma discharge*, J. Phys. D: Appl. Phys. 42 (2009) 135209

[25] J.A. Santiago et al., *Adhesion enhancement of DLC hard coatings by HiPIMS metal ion etching pretreatment*, Surface and Coatings Technology 349 (2018) 787-796

[26] CEN/TS 1071-11:2005: Advanced technical ceramics: Methods of test for ceramic coatings, Part 11: Determination of internal stress by the Stoney formula

[27] L. Yate et al., *Effect of the bias voltage on the structure of nc-CrC/aC:H coatings with high carbon content*, Surface and Coatings Technology 206 (2012) 2877-2883

[28] J.A. Leavitt and L.C. McIntyre, Jr., *Non-Rutherford 4He cross sections for ion beam analysis*, Nuclear Instruments and Methods in Physics Research B56/57 (1991) 734-739

[29] M. Mayer, SIMNRA, Max Planck Institut für Plasmaphysik, n.d.

[30] A.C. Ferrari et al., *Interpretation of Raman spectra of disordered and amorphous carbon*, Physical Review B 62, 16 (2000) 11089-11103

[31] S. Urbonaite et al., *EELS studies of carbide derived carbons*, Carbon 45 (2007) 2047-2053

[32] X. Zhang et al., *Practical aspects of the quantification of sp2-hybridized carbon atoms in diamond-like carbon by electron energy loss spectroscopy*, Carbon 102 (2016) 198-207

[33] W.C. Oliver, G.M. Pharr, *An improved technique for determining hardness and elastic modulus using load and displacement sensing indentation experiments*, Journal of Materials Research 7 (1992) 1564-1583

[34] S. Berg, I. Katardijev, *Resputtering effects during ion beam assisted deposition and the sputter yield amplification effect*, Surface and Coatings Technology 84 (1996) 353-362

[35] C. Nender et al., *Numerical and experimental studies of the sputter yield amplification effect*, Radiation Effects and Defects in Solids 130-131 (1994) 281-291

[36] S. Berg et al., *Atom assisted sputtering yield amplification*, Journal of Vacuum Science and Technology A 10 (1992) 1592

[37] A. Anders et al., *Drifting localization of ionization runaway: Unraveling the nature of anomalous transport in high power impulse magnetron sputtering*, J. Phys. D: Appl. Phys. 45 (2012) 012003

[38] A. Anders, *Self-sputtering runaway in high power impulse magnetron sputtering: The role of secondary electrons and multiply charged metal ions*, Applied Physics Letters 92 (2008) 201501

[39] R. Daniel et al., *The origin of stresses in magnetron-sputtered thin films with zone T structures*, Acta Materalia 58 (2010) 2621-2633

[40] C. Corbella et al., *Structure of diamond-like carbon films containing transition metals deposited by reactive magnetron sputtering*, 14 (2005) 1103-1107

[41] J.H. Choi et al., *Stress reduction behavior in metal-incorporated amorphous carbon films: first-principles approach*, Journal of Physics: Conference Series 29 (2006) 155-158

[42] J. Schwan et al., *Tetrahedral amorphous carbon films prepared by magnetron sputtering and dc ion plating*, Journal of Applied Physics 79 (1996) 1416-1422

[43] J. Schwan et al., *Raman spectroscopy on amorphous carbon films*, Journal of Applied Physics 80 (1996) 440

[44] A.C. Ferrari, J. Robertson, *Interpretation of Raman spectra of disordered and amorphous carbon*, Phys. Rev. B 61 (2000) 14095

[45] C. Adelhelm et al., Influence of doping (Ti, V, Zr, W) and annealing on the sp2 carbon structure of amorphous carbon films, Journal of Applied Physics 105 (2009) 033522

[46] S. Prawer et al., *Raman spectroscopy of diamond and doped diamond*, Diamond and Related Materials 5 (1996) 433-438

[47] R. Arenal, *Clustering of aromatic rings in near-frictionless hydrogenated amorphous carbon films probed using multiwavelength Raman spectroscopy*, Appl. Phys. Lett. 91 (2007) 211903

[48] L. Lajaunie et al., *Advanced spectroscopic analyses on aC:H materials: Revisiting the*

EELS characterization and its coupling with multi-wavelength Raman spectroscopy, Carbon 112 (2017) 149-161

[49] X. Fan et al., *Z-contrast imaging and electron energy-loss spectroscopy analysis of chromium-doped diamond-like carbon films*, Appl. Phys. Lett. 75 (1999) 18

[50] C. Adelhelm et al., *Investigation of metal distribution and carbide crystallite formation in metal-doped carbon films (aC:Me, Me= Ti, V, Zr, W) with low metal content*, Surface and Coatings Technology 205 (2011) 4335-4342

[51] D.O.I. Kazuya et al., *Preparation of crystalline chromium carbide thin films synthesized by pulsed Nd:YAG laser deposition*, Mater. Res. Soc. Symp. 617 (2000) J7.8.1

[52] J. Robertson, *Deposition mechanisms for promoting sp3 bonding in diamond-like carbon*, Diamond and Related Materials, 5-7 (1993) 984-989

[53] A. Leyland, A. Matthews, *On the significance of the H/E ratio in wear control: a nanocomposite coating approach to optimized tribological behavior*, Wear, 246 (2000) 1-11

[54] J. Musil et al., *Relationships between hardness, Young's modulus and elastic recovery in hard nanocomposite coatings*, Surface and Coatings Technology 154 (2002) 304-313

[55] M. Rouhani et al., *In-situ thermal stability analysis of amorphous carbon films with different sp3 contents*, Carbon 130 (2018) 401-409

[56] S. Neuville, A. Matthews, *A perspective on the optimisation of hard carbon and related coatings for engineering applications*, Thin Solid Films 515 (2007) 6619.

[57] S. Neuville, *Carbon Structure Analysis With Differentiated Raman Spectroscopy*, Lambert Academic Press, 2014

[58] S. Neuville, *Quantum electronic mechanisms of atomic rearrangements during growth of hard carbon films*, Surface & Coatings Technology 206 (2011) 703–726

[59] J. Wagner, et al., Proceedings by, in: P. Koidl, P. 197. Oelhafen (Eds.), Les editions de la Physique, 1987, p. 219.

[60] J.M. Marco et al., SVC Proceedings 2015; dx.doi.org/10.14332/svc15.proc.1935

[61] T.B. Ma et al., *Molecular dynamics simulation of shear-induced graphitization of amorphous carbon films*, 47 (2009) 1953-1957

[62] T. Haque et al., *The role of abrasive particle size on the wear of diamond-like carbon coatings*, Wear 302 (2013) 882-889

List of tables

Tables

Table 1. Brief summary of DLC and Cr-doped DLC coatings deposition parameters, Cr content, deposition rate and, residual stress

Sample	Power Cr (W)	Frequency (Hz)	Cr content (at. %) (XPS)	Cr content (at. %) (RBS)	Dep. rate (nm/h)	Residual stress (GPa)
DLC	---	---	---	---	200	-3,75
DLC:Cr_1	25	15	3	---	210	-2,75
DLC:Cr_2	25	50	9	9	235	-1,5
DLC:Cr_3	100	100	20	18	265	-1,25

Table 2. Overview of the mechanical properties measured for the studied DLC and Cr-doped DLC coatings

Sample	Hardness (GPa)	Reduced elastic modulus (GPa)	H/E	H^3/E^2
DLC	31.4 ± 2.7	245 ± 16	0.128	0.516
DLC:Cr_1	29.2 ± 2.6	236 ± 14	0.124	0.447
DLC:Cr_2	17.6 ± 1.4	166 ± 7	0.106	0.198
DLC:Cr_3	15.4 ± 1.2	144 ± 7	0.106	0.176

Table 3. Evolution of the I_D/I_G ratio and surface roughness with temperature for the studied DLC and Cr-doped DLC coatings

Sample	sp^3	I_D/I_G @RT	I_D/I_G @400ºC	Roughness @RT	Roughness @400ºC
DLC	27±3	0.43	1.15	4.7	5.2
DLC:Cr_1	28±5	0.62	1.34	5.3	6.7
DLC:Cr_2	24±3	0.76	1.73	6.4	17.2
DLC:Cr_3	---	1.32	2.12	6.2	23.4

List of figure captions

Figure 1

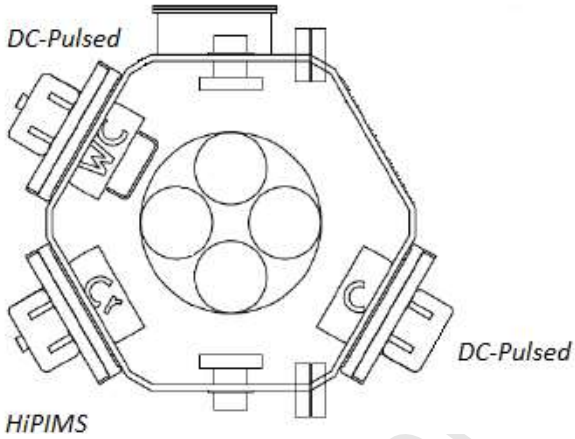

Figure 2

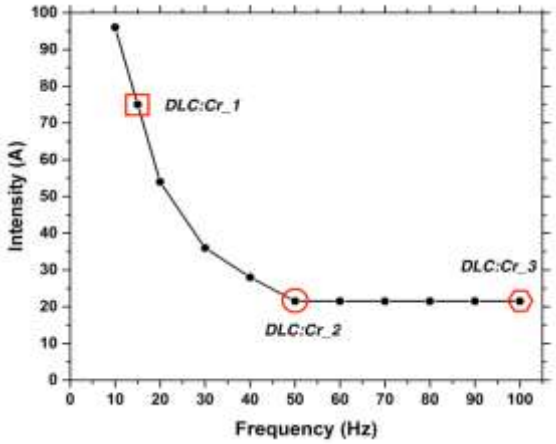

Figure 3

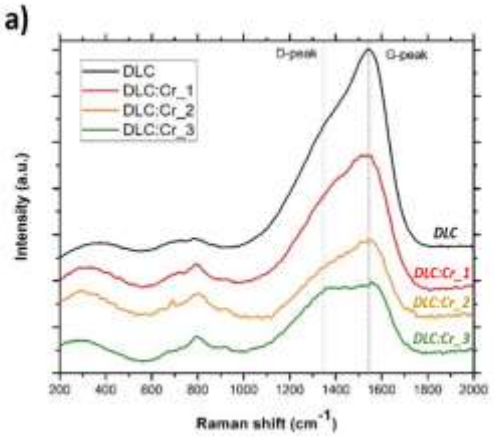

Figure 4

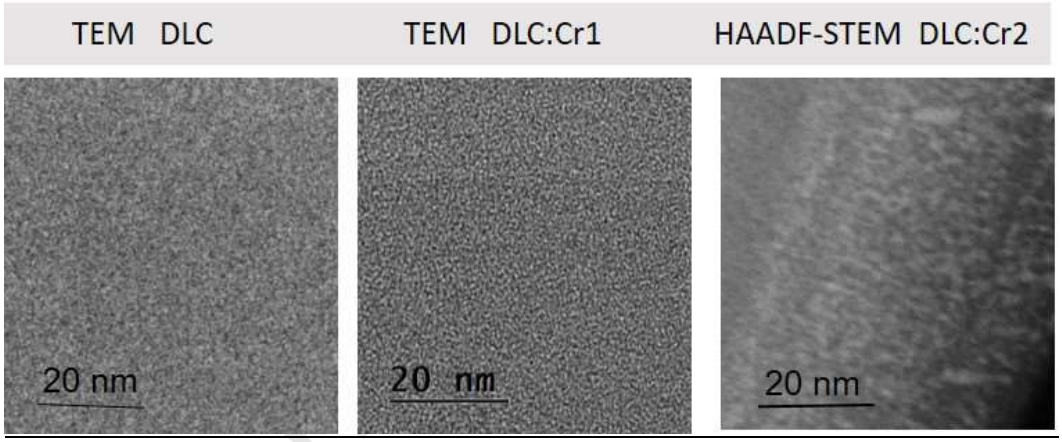

Figure 5

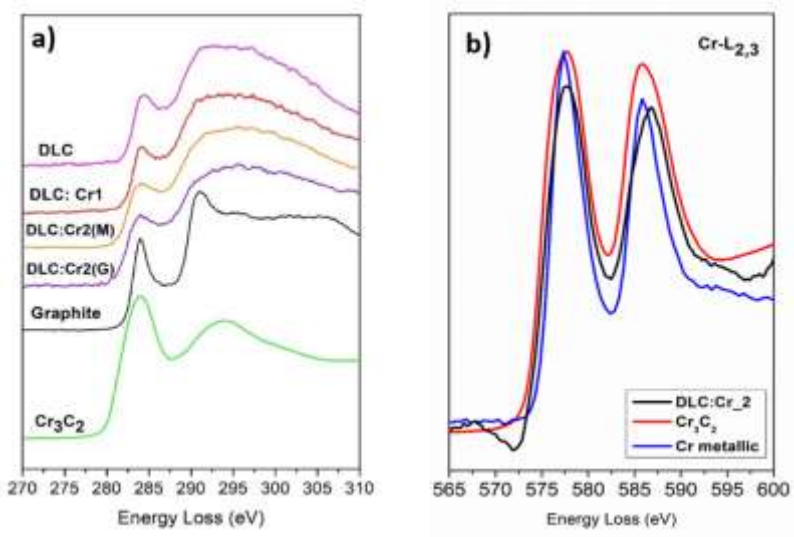

Figure 6

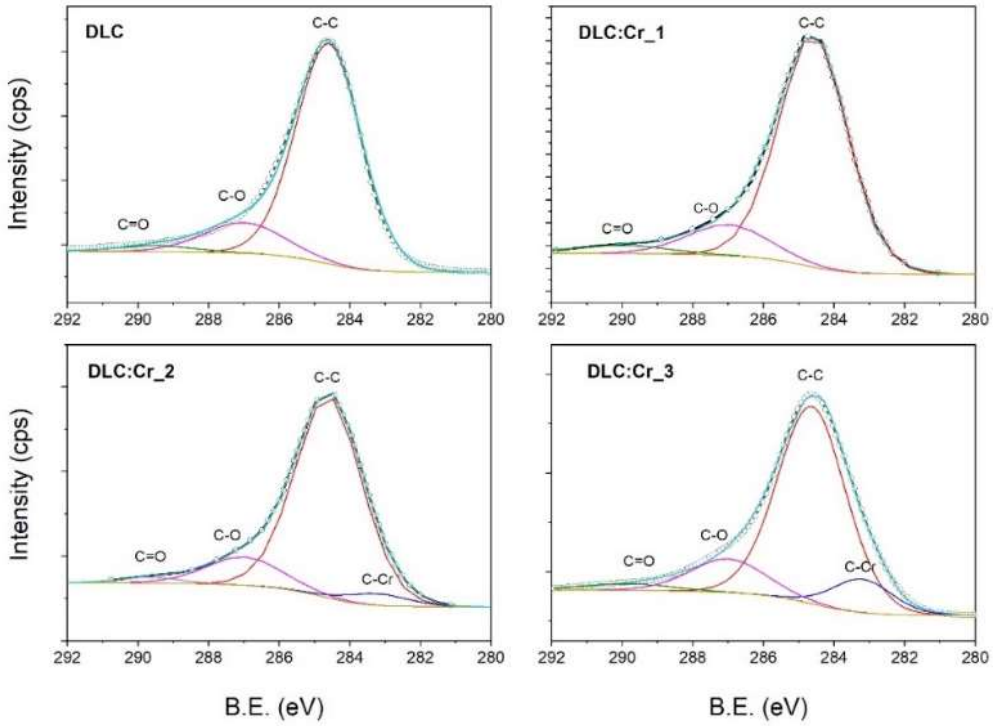

Figure 7

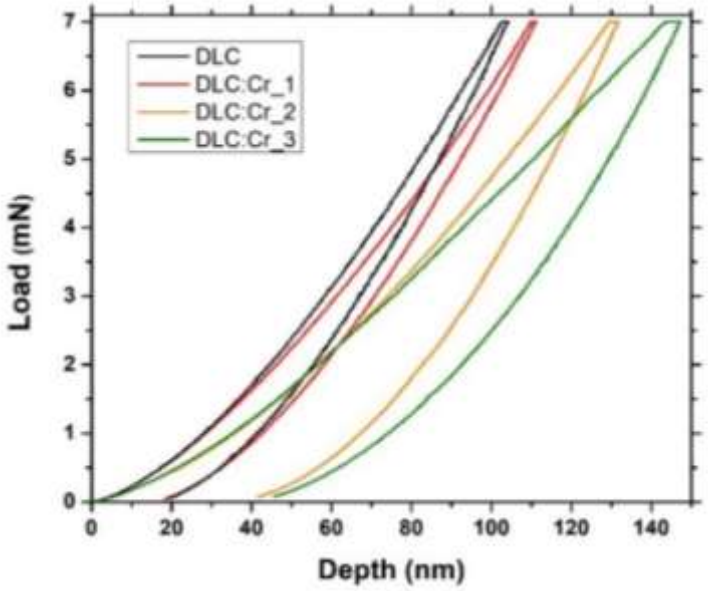

Figure 8

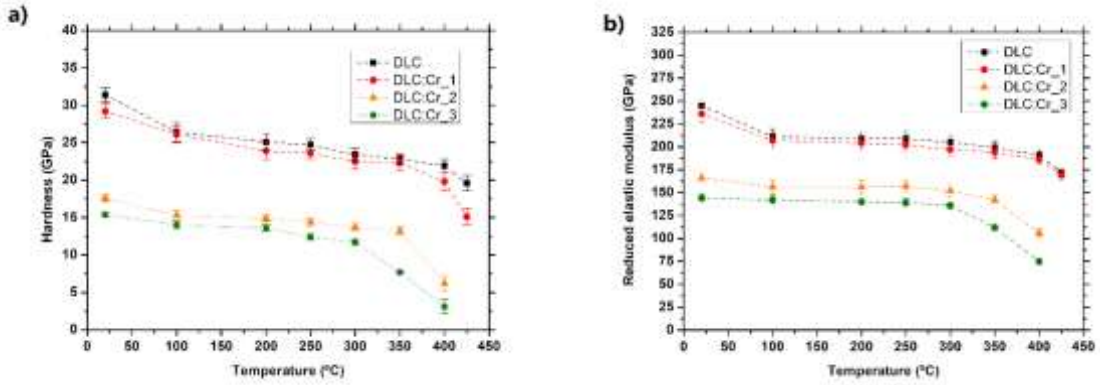

Figure 9

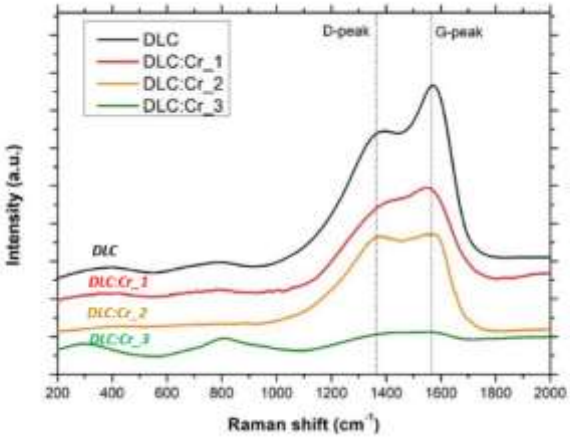

Figure 10

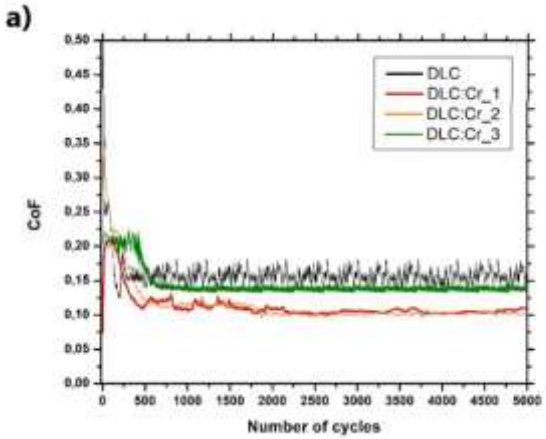

Figure 11

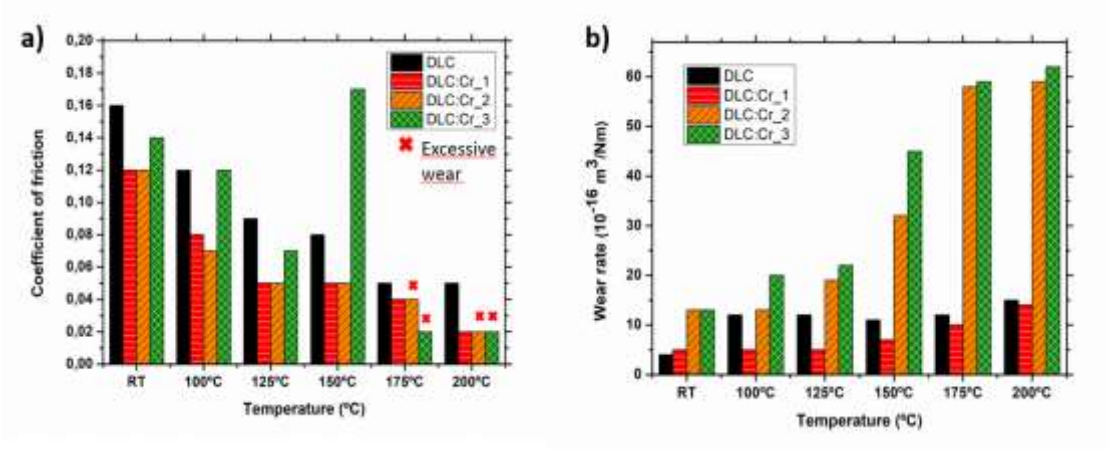

Figure 12

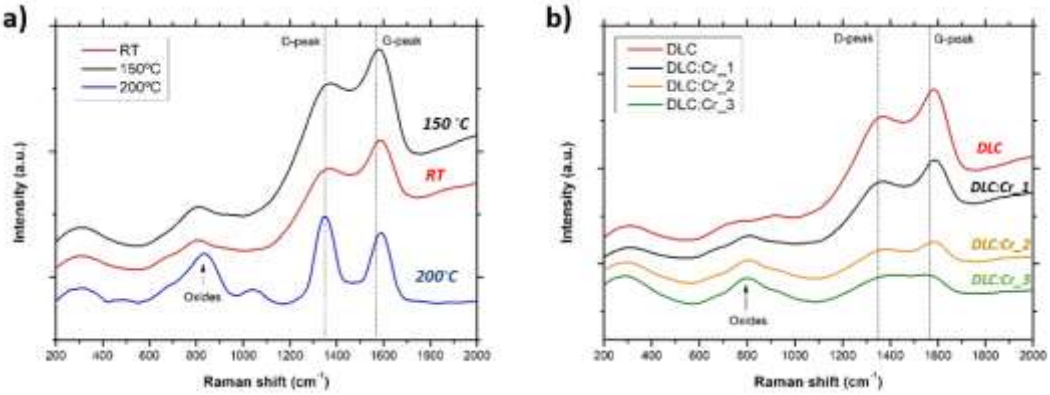

Figure 13

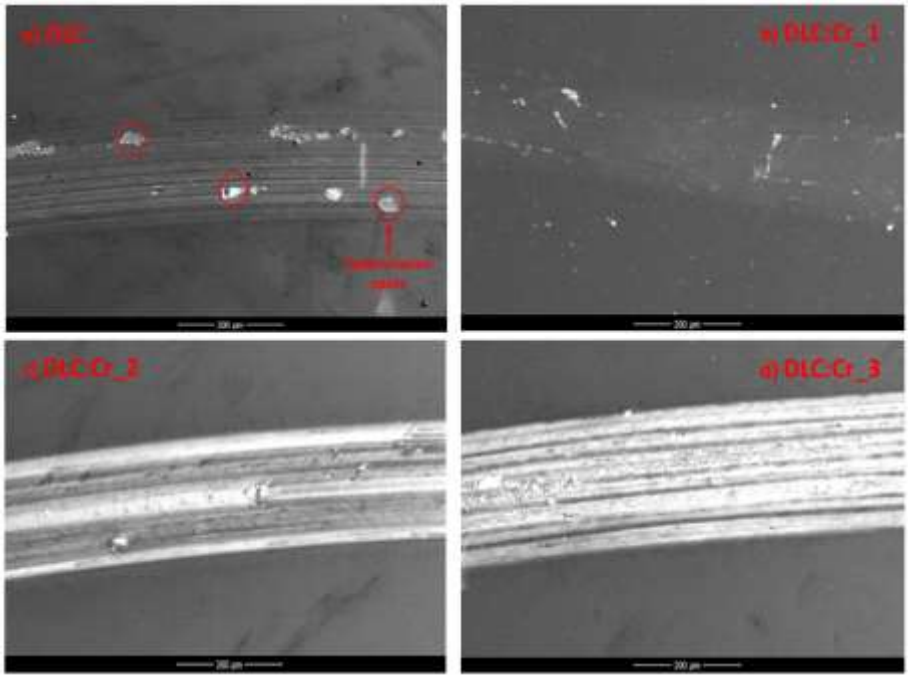

Highlights

1. Cr-doped DLC coatings were co-deposited by low-frequency/high current HiPIMS method.

2. Cr doping by low frequency HiPIMS preserves DLC sp^3 content and reduces compressive stress.

3. Low at. % Cr-doped DLC exhibit high hardness (up to 29 GPa) and delayed graphitization (up to 400 C).

4. Low at. % Cr-doped DLC presents enhanced tribological behaviour at high temperatures by creating stable tribolayers.